Eliminating Biases in Quantitative Infrared Thermography: Stray Light and Readout Corrections for Accurate Heat-Flux Measurements in Hypersonic Flows

by J. Lunte*, E. Schülein*

* German Aerospace Center (DLR), Institute of Aerodynamics and Flow Technology, Department of High Speed Configurations, Bunsenstr. 10, 37073 Göttingen, Germany, jens.lunte@dlr.de

Abstract

Accurate temperature measurements are essential for determining heat transfer rates by quantitative infrared thermography. Previous wind tunnel studies revealed systematic errors, as temperature changes confined to part of the field of view affected the thermosignal in the remaining image regions. Reflections were excluded as the cause. Using a black body emitter with a test specimen confirmed this mutual pixel influence in a specifically recreated laboratory experiment. Analysis identified two error sources known from photography as stray light and readout artefacts. Based on the obtained data, simplified correction models were developed, systematically validated and demonstrated on the wind tunnel data.

1. Introduction

Infrared thermography is an established non-intrusive method for measuring surface temperature [1, 2]. The radiation emitted from the surface of interest is imaged through a camera lens onto a focal plane array, consisting of up to millions of individual detector elements. The detector elements generate an output signal, which is approximately proportional to the impinged radiation [1] and digitized by an integrated readout circuit utilising analog-to-digital converters. As each camera pixel is embodied by a separate sensor with its specific radiation response, the sensor chip requires a non-uniformity correction [3] to equalise the output signal between the pixels and a temperature calibration to convert the signal to surface temperature values.

To establish a robust calibration methodology, prior studies [1, 2] systematically analysed the composition of detectable radiation for infrared measurement systems. The structured decomposition of incident radiation also serves as the foundation for explaining and correcting observed imaging artefacts, including the Narcissus effect [1], translucent surface materials [4], and the angular dependence of surface emissivity [2]. The greatest uncertainties for wind tunnel measurement often lie in the insufficiently known emission, reflection and transmission coefficients of all surfaces involved and the optical components (lenses and windows) located between the camera sensor and the test object. These effects can be mitigated through the judicious selection of components and subsequently corrected during data post-processing.

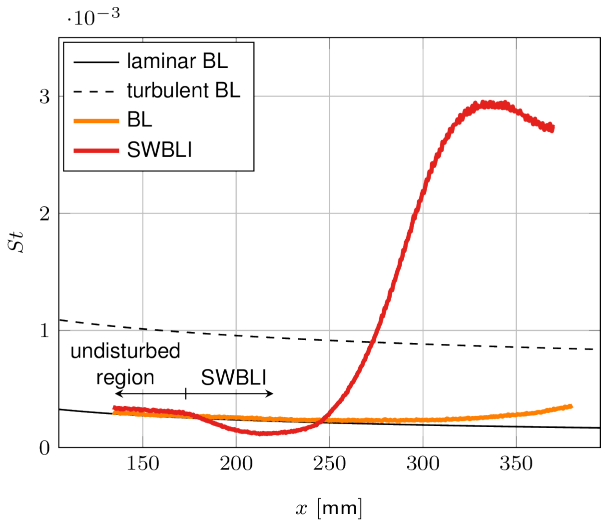

(a) *Streamwise St distribution on the flat plate with and without a SWBLI.*

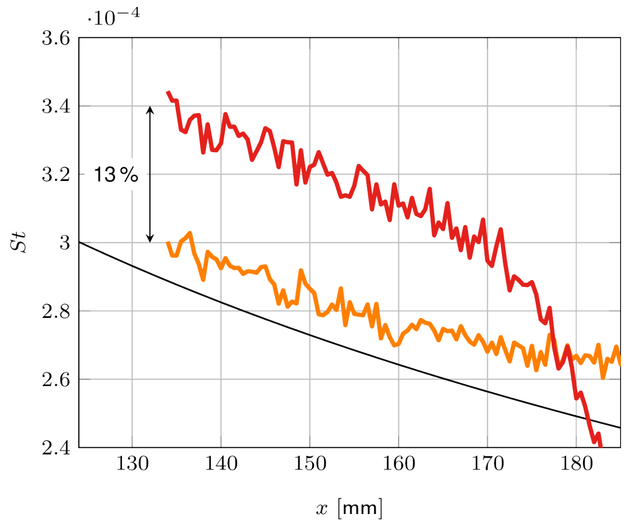

(b) *Enlarged view of figure 1a.*

Fig. 1. *Visualisation of the systematic measurement errors in the St distributions.*

Although the quantitative infrared thermography (QIRT) setup along with the evaluation methodology [5, 6] have been well-established at the Ludwieg-Tube wind tunnel in Göttingen (RWG), an unexpected systematic discrepancy between the measured heat-flux distributions was observed. The discrepancy is displayed in figure 1, which shows the experimental Stanton number (St) distribution along a flat plate at the Mach 6 flow conditions together with two theoretical curves for the laminar and turbulent boundary layer derived from idealised assumptions. Besides the undisturbed flow around the plate, a displacement body was mounted above the plate to generate a 2D impinging shock-wave/boundary-layer interaction (SWBLI). Details about the experiments and the flow physics of SWBLI can be found in [6, 7], but are beyond the scope of the current paper. For the current paper, it is sufficient to notice that the SWBLI causes a drastic increase in the heat transfer rates and therefore leads to different surface temperature levels in the field of view (FOV) of the camera. According to theory and numerical simulations, the heat transfer rates upstream of the SWBLI should match those of the undisturbed boundary layer (BL). But as the magnified plot in figure 1b shows, the measured heat fluxes are 13 % higher, which is significant compared to the statistical error of under 2 % [7].

The deficiency in the undisturbed region was the incentive to investigate the measured values of our infrared camera in more detail by replicating the key components of the experiment in a laboratory setup. Dedicated tests revealed two additional systematic imaging artefacts, which showed similarities to the stray light and readout artefacts known from photography. After highlighting the individual artefacts and discussing their respective cause, the obtained laboratory database was used to develop and calibrate heuristic correction models. The success of the correction models was then demonstrated using the available heat transfer measurements from wind tunnel campaign.

2. Experimental Program

2.1 Investigation of stray light and readout artefact

The systematic investigation of the errors in our heat transfer measurements takes place by laboratory experiments, which emulates the situation in the wind tunnel. The emulation includes the identical optical components and the replication of the higher temperature level in a part of the camera's field of view as a consequence of the steep heat transfer increase (see figure 1a). The arrangement of the optical components is sketched in figure 2.

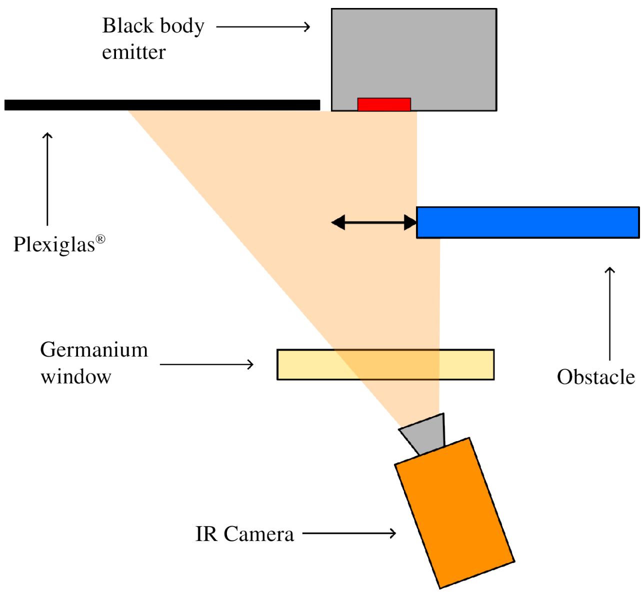

Fig. 2. *Sketch of laboratory tests.*

A black Plexiglas® plate serves as the measurement surface for the investigations and is suitable for the determination of surface temperatures by means of an infrared camera due to its measured emissivity of $\varepsilon = 0.96$. Like at the wind tunnel, the radiation of the Plexiglas® passes through a germanium window (transmissivity of 94 %) and impinges at an angle of approximatly 20° onto the 25 mm objective of the infrared camera system *IRCAM EQUUS 327kL*. The camera has a 640 x 512 pixel FPA-sensor and detects radiation in the spectral range of 8.0 µm - 9.4 µm. The analog-digital-converter digitizes the signal with 14-bit resolution, yielding 16 384 discrete intensity values C. Within the camera's field of view, the black body emitter *BR400* is positioned next to the Plexiglas® plate. The *BR400* was selected for its aperture of 128 mm and set to a temperature of $T = 150\,°C$.

In each laboratory test, 3 image sequences were recorded in which a fabric-covered styrofoam plate was gradually moved into and out of the camera's FOV to gradually cover the aperture of the black body emitter. After the series of 3 image sequences, the infrared camera was rotated by 90° around its longitudinal axis and the coverage test was repeated. The rotation changes the image axis along which the camera's internal line-by-line pixel readout is performed. Each image in the sequences is an average of 100 frames acquired at a frequency of 105 Hz with an exposure time of 100 µs.

2.2 Temperature calibration of intensity levels

To assign the intensity values of the camera to a temperature, a calibration is necessary. For this purpose, the infrared camera looks through the germanium window directly into the aperture of the black body emitter *Hyperion R982*, on which the emitter temperature was increased incrementally and recorded by the camera. The black body emitter was changed for the calibration process due to its better emissivity ($\varepsilon_{\text{R982}} > 0.995$) and temperature stability of $\pm 0.1\,°\text{C}$.

3. Results and Discussion

Figure 3 shows the camera FOV with the Plexiglas® area on the left and the blackbody emitter on the right. To visualise details in the thermal image despite its large dynamic range, the measured intensity values C of the pixels are displayed using non-linear scaling. The investigated region of interest (ROI) is marked. To quantify the consistency, the temporal standard deviation of each pixel was calculated and averaged over the ROI (σ_{ROI}). The statistical noise of $\sigma_{\text{ROI}} = 1.3$ Counts was determined as the reference value.

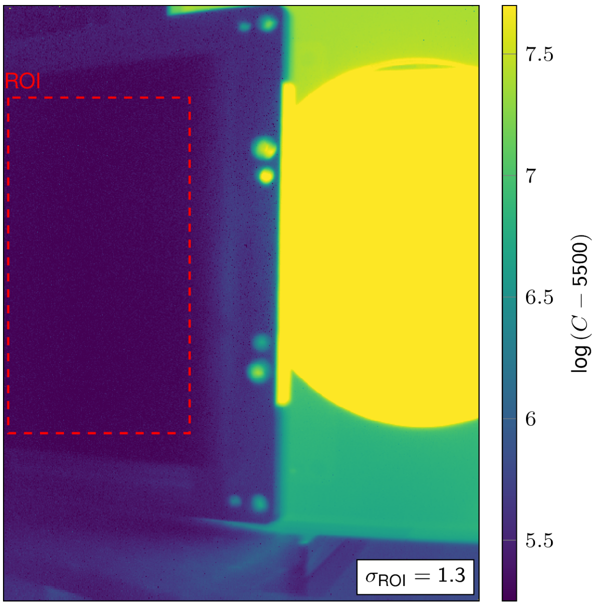

Fig. 3. *Camera FOV for the laboratory tests without obstacle*

3.1 Stray light artefact

The recording time of each test sequence lasted approximately 120 seconds. A time period in which the surface temperature of the Plexiglas® does not change. Increased obstruction of the black body aperture by the obstacle induces a monotonic decrease in the detected radiometric intensity level within the ROI, despite a constant surface temperature. The calculation of difference images, referenced to the initial frame, reveal this artefact by isolating the obstruction-induced radiometric deviations from the verified constant-temperature baseline. Figure 4a depicts a difference image, where the aperture of the black body emitter is approximately 60 % obscured and indicates a nearly uniform decrease of the ΔC within the ROI.

A known challenge in infrared measurement results from the interaction of each body with the radiation according to its emissivity, reflectivity and transmissivity. One possible cause of error are reflections on the Plexiglas® surface. So 4 % of the measured radiation power coming from the Plexiglas® surface originates not from the Plexiglas® itself, but from the environment. Via a cascade of reflections, the black body emitter contributes to a certain amount directly to the measured radiant power. If the black body emitter becomes obscured, the amount of reflection-based radiation is also reduced.

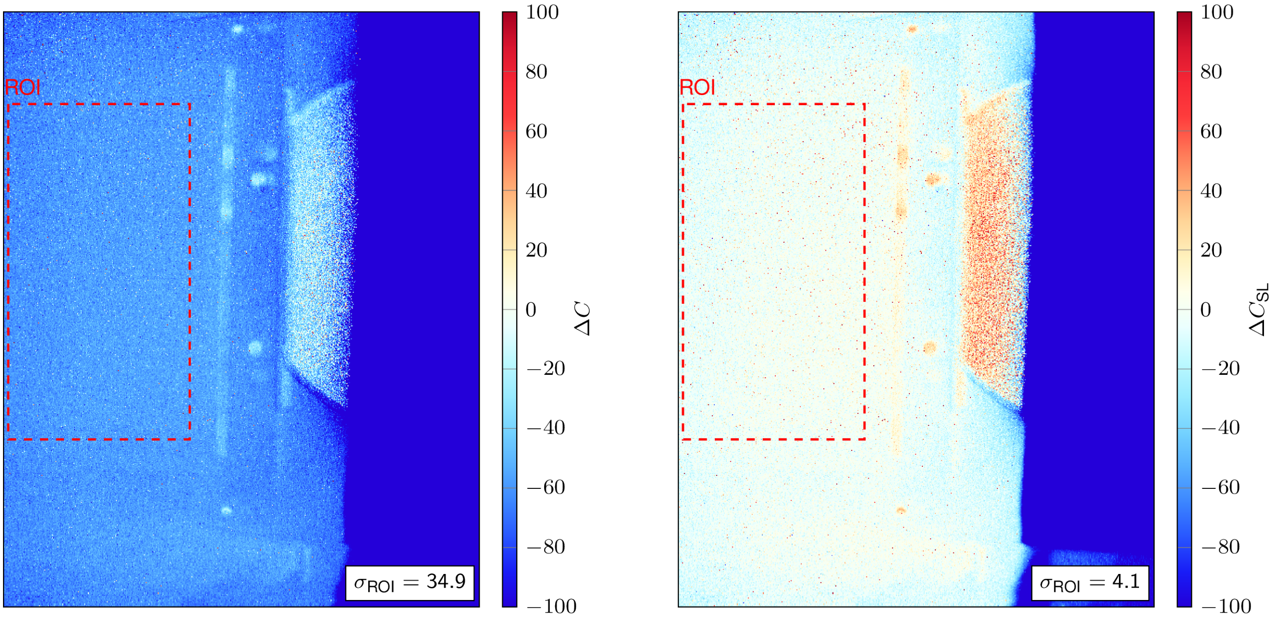

(a) *The stray light artefact reduces the count values in the image uniformly.*

(b) *After the stray light correction, the signal in the ROI remains almost constant during the sequence.*

Fig. 4. *Visualisation of the stray light artefact at approximately 60 % masking.*

After an assessment of the beam trajectory in the specific laboratory situation, the authors consider the outlined reflection-based influence of the black body emitter on the total radiation to be insufficient to explain the measured ΔC values. In a verification test, the black body emitter was pulled sideways out of the field of view, which changed the beam path of the reflections only insignificantly. During the extraction, the measured thermosignal of the Plexiglas® surface decreased in an analogous way as when the black body emitter was covered by the obstacle. The verification test indicates that the ΔC correlate with the number of covered pixels.

Another known image artefact is stray light [8, 9], which refers to any light that impinges on the optical detector that is not part of the ideal focused light bundle. Stray light enters a camera system in various forms, each degrading the image quality in a distinct way. A non-exhaustive list of stray light causes includes multiple reflections between lens surfaces (known as lens flares), light scattering on the components of the camera system and light leaks into the camera system.

To compensate the impact of these contributions on the sensor response, the system is described mathematically as follows. The sensor output is approximately proportional to the incident radiant power [1]. The incident radiant power originates from the entire half-space and shall be divided into three parts for the correction model: The radiation power from the focused measurement point P_{mp}, from the environment P_{env}, and from the stray light P_{SL}. In an ideal measurement device P_{mp} is the only contribution, but in a real device P_{mp} has at least the biggest share. P_{env} shall not only include the reflections on the measurement surface but also the radiation from the inside walls of the IR-Camera [1] and further miscellaneous contributions like the emitted radiation from the air and lenses. P_{SL} shall contain the radiation, which we identified as the measurement error in figure 4a. In total the measured intensity values can be described as

$$C = a_1 P_{\text{mp}} + a_2 P_{\text{env}} + a_3 P_{\text{SL}} + b, \tag{1}$$

where a_1, a_2, a_3 and b are placeholder constants, which embody the combination of the emissivity, reflectivity and transmissivity coefficients of the various involved objects. A more detailed breakdown of the total radiation power and the combination of the coefficients can be found in [1]. In the current paper it suffices to handle them as individual constants. The difference images were obtained by pixel-wise subtraction of the initial frame C^0 from the sequence. For pixels inside the ROI the variables P_{mp} as well as P_{env} stay constant as the time interval is to short for a significant temperature change, which leads to

$$\Delta C_{\text{ROI}} = C_{\text{ROI}} - C^0_{\text{ROI}} = a_3 \left(P_{\text{SL}} - P^0_{\text{SL}} \right). \tag{2}$$

As mentioned earlier, the influence of stray light does not seem to depend on the distance of the ROI pixels from the edge of the hotspot, but on size of the hotspot as well as on the mean temperature difference in the field of view. The uniform change of the thermosignal in figure 4a, leads to the assumption that $a_3 P_{\mathrm{SL}}$ is proportional to the mean intensity value of the image C_{mean}. With the new proportionality constant l, equation 2 can now be written as

$$\Delta C_{\mathrm{ROI}} = l\left(C_{\mathrm{mean}} - C^{0}_{\mathrm{mean}}\right) = l\Delta C_{\mathrm{mean}}. \tag{3}$$

The assumptions required for deriving equation 3 can be validated by checking the correlation with the measured data. For the verification, the ΔC_{ROI} are plotted versus ΔC_{mean} in figure 5. As this evaluation is conducted pixelwise, each data point is plotted partially transparent to give an impression of the frequency distribution and the main trend. The data points follow a line through the origin as predicted by equation 3 and can be used to determine the proportionality constant l.

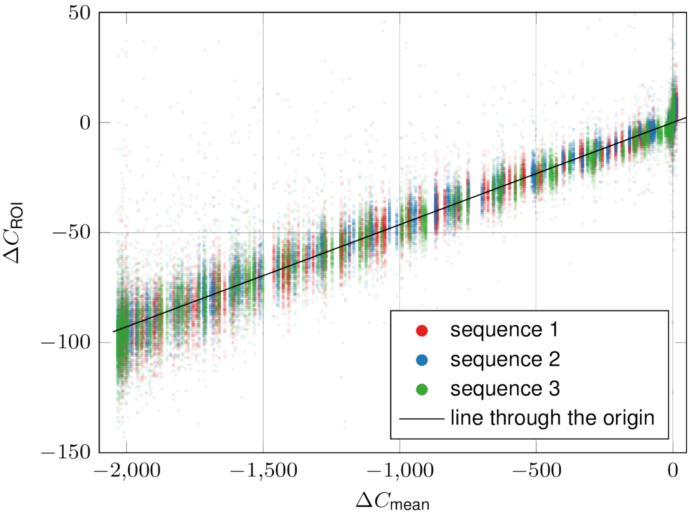

Fig. 5. *Correlation of the stray light artefact with ΔC_{mean}.*

The experimental data can now be corrected for the stray light artefact by replacing $a_3 P_{\mathrm{SL}}$ in equation 1 with lC_{mean} and rearranging it to

$$C_{\mathrm{SL}} := C - lC_{\mathrm{mean}}. \tag{4}$$

After the correction the intensity values are nearly constant during the sequence as can be seen in figure 4b. The temporal standard deviation σ_{ROI} is drastically reduced and in the same order of magnitude as the statistical noise.

3.2 Readout artefact

In the second series of experiments, the infrared camera was rotated around its longitudinal axis by 90°, so the readout lines now contain both the Plexiglas® surface and the black body aperture. Figure 6a shows that the original intensity values vary during the recorded sequence. But even after conducting the stray light correction (eq. 4) the difference signal in the ROI is not zero (figure 6b), although the pixels in the rows above and below the aperture of the black body emitter (regions A and B) deviate less.

The stray light correction fails in regions, where the rows of the camera undergo a significant change of the measurement signal during the recorded sequence. As this artefact correlates strongly with the readout direction of the camera, the readout mechanism seems unable to digitize the signal of each pixel individually. While the reason for the origin of the readout artefacts depend on the specific sensor design, comparable artefacts are known for CCD sensors as smear [10] and can also occur with CMOS sensors [11, 12]. The *IRCAM EQUUS 327kL* uses a readout integrated circuit (ROIC), which can suffer from crosstalk effects [13]. A request to *IRCAM GmbH* for detailed information about the implemented ROIC for further analysis was declined because the ROIC is not in the public domain. Without the specific structure of the ROIC, a heuristic approach for compensation of the readout artefact is carried out.

For modelling, each measured intensity value should be composed of the true intensity value and a portion r of the mean intensity value along the readout line $\bar{C}_{\mathrm{rol}}$:

$$C = C_{\mathrm{true}} + r\bar{C}_{\mathrm{rol}}. \tag{5}$$

During the recorded sequence, the C_{true} in the ROI are constant. Thus, calculating the difference images leads to

$$\Delta C = r\Delta\bar{C}_{\mathrm{rol}}. \tag{6}$$

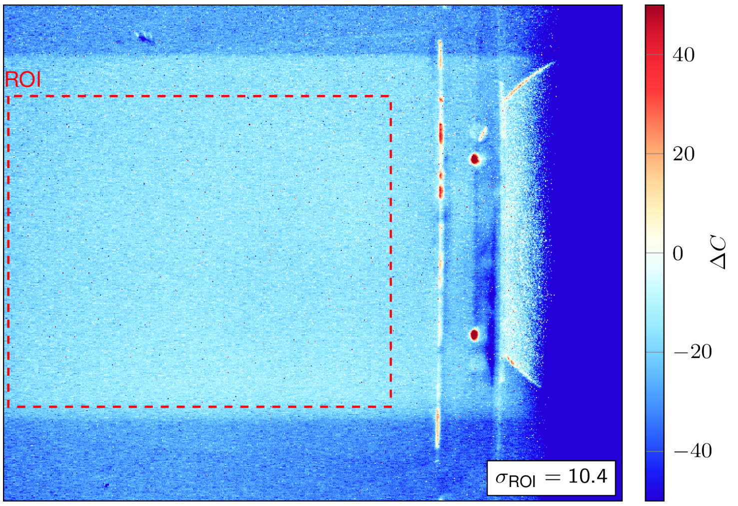

(a) *Uncorrected differential image of the camera.*

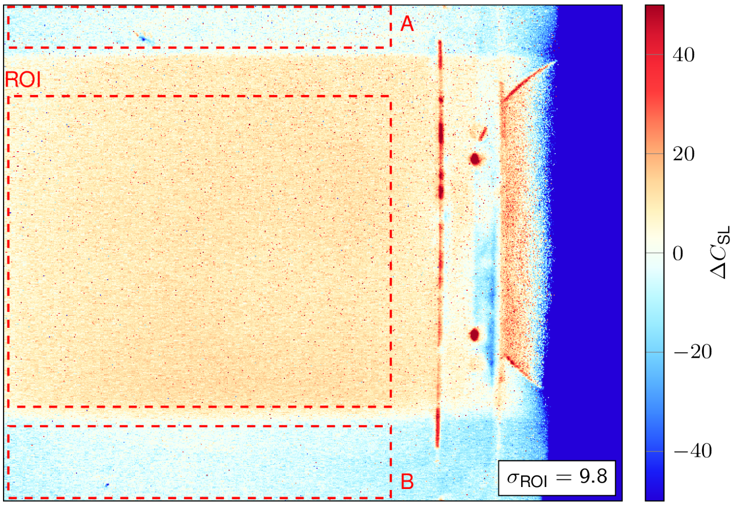

(b) *The stray light correction is not sufficient to stabilize the signal in the ROI.*

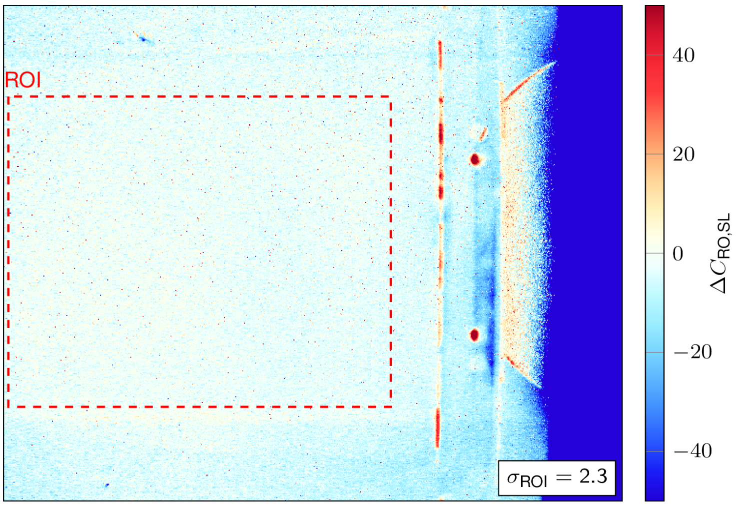

(c) *The correction of the readout and stray light artefact leads to a constant measurement signal in the ROI.*

Fig. 6. *Visualisation of the readout artefact*

To investigate the scaling factor r the stray light corrected data is used and the quotient $\Delta C_{\text{SL}}/\Delta\bar{C}_{\text{row,SL}}$ is plotted against the pixel position j of the readout line in figure 7. In the diagram $N_{1/2}$ denotes the center of the readout line and pixels above $j - N_{1/2} > 80$ are omitted from the plot, because they are depicting the black body emitter and can not be analysed.

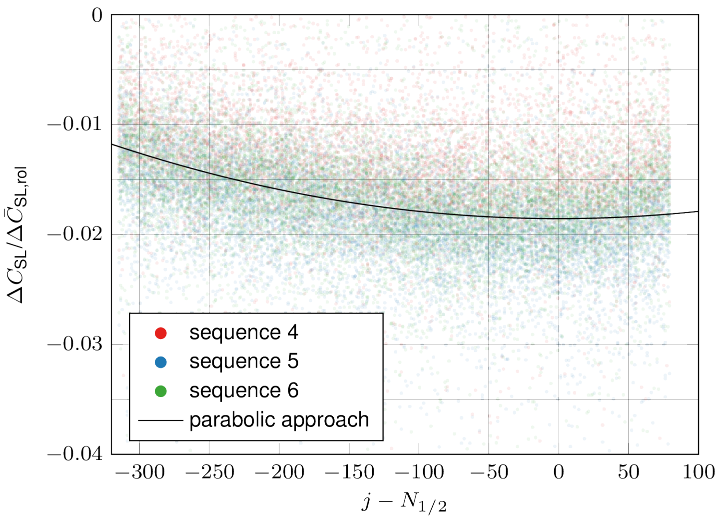

Fig. 7. *Correlation of the readout error.*

Although the distribution of the data points is scattered, the main trend exhibits a dependence of the scaling factor on the position in the readout line. The absolute position of the pixel seems to be the relevant quantity, because the scaling factor performs a trend reversal at $j - N_{1/2} \approx 0$ although the pixels $j - N_{1/2} > 0$ are much closer to the obscured pixels.

A correction of the main trends suffice to reduce the measurement error of the camera significantly. To keep the corrections simple and robust, a parabolic approach is chosen for the scaling factor:

$$r = r_1 \left(1 + r_2 \frac{(j - N_{1/2})^2}{N^2}\right) \tag{7}$$

To correct the readout artefact the mapping

$$C_{\text{RO}} \coloneqq C - r_1 \left(1 + r_2 \frac{(j - N_{1/2})^2}{N^2}\right) \bar{C}_{\text{rol}} \tag{8}$$

is applied. Methodically, the readout of the signals is the last step in the process chain of the camera. The correction of the observed errors must therefore be performed in reverse order. This means the readout error must be corrected before the stray light error. But an independent determination of the correction factors r_1 and r_2 is not possible. To overcome this problem, a least square fit is set up in which the measurement data is first processed with equation 8 and afterwards with equation 4. The fit parameter r_1, r_2 and l are optimized to reduce σ_{ROI} and for the starting values the coefficients of the preliminary curves shown in figure 5 and 7 were chosen. The results for our specific camera are listed in table 1 and figure 6c shows the corrected measurement data. With both corrections σ_{ROI} got reduced to a comparable level of the statistical noise.

3.3 Temperature calibration

A new calibration is required to convert the corrected intensity levels to a temperature. Therefore, the signal of the aperture of the black body emitter was corrected for the readout and stray light error as well as averaged. Figure 8 shows the calibration data for the different reference temperatures of the black body. Due to both corrections the signal is significantly reduced. According to the Stefan-Boltzmann law, the total radiated power of a unit area is given by σT^4 for a black body with the Stefan-Boltzmann constant $\sigma = 5.67 \cdot 10^{-8}\,\text{W/m}^2\text{K}^4$. Although the infrared camera can only detect a narrow part of the full wavelength spectrum, the calibration data shall be approximated by $k_1\sigma T^4 + k_2$. The determined values for k_1 and k_2 are listed in table 1.

Table 1. *Fit results for the investigated infrared camera*

parameter	fit result
l	$4.744 \cdot 10^{-2}$
r_1	$-1.999 \cdot 10^{-2}$
r_2	-1.364
k_1	$6.293\,\mathrm{m^2/W}$
k_2	2814.71

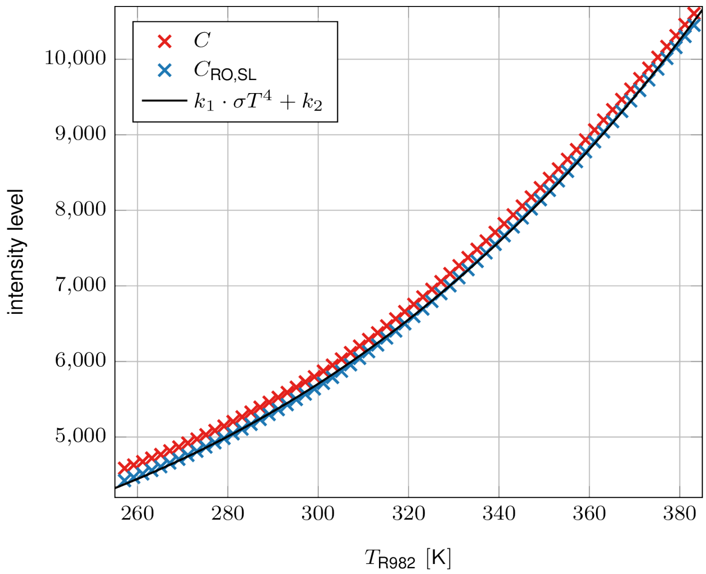

Fig. 8. *Temperature calibration for the corrected intensity levels.*

3.4 Impact of the corrections

The two correction approaches successfully reduced the observed systematic errors in the laboratory tests. Their effect on real wind tunnel data and heat flux density determination is demonstrated for the initial case of figure 1. With the proposed corrections, the SWBLI St-distribution (figure 9) now aligns with the undisturbed flow situation upstream of the interaction, resolving the systematic measurement error. The corrections have an insignificant effect on the region with high heat fluxes ($x > 270\,\mathrm{mm}$), since the temperature change between consecutive images outweighs the correction magnitude. The heat transfer values of the undisturbed boundary layer remain almost unaffected, as temperature differences in the FOV are marginal.

4. Conclusion

In a special calibration study, the experimental setup of a previous wind tunnel experiment was replicated in the laboratory to investigate the causes and extent of systematic errors in quantitative heat flux measurements using infrared thermography that had occurred during data analysis. Basic tests exposed two distinct image artefacts, that cause a systematic error in the detected thermosignal. One artefact was attributed to stray light impinging on the camera sensor, while the other error was caused by the readout mechanism of the camera system.

For both artefacts, correction approaches were developed and unknown parameters were determined based on the recorded laboratory dataset. After a successful demonstration of the correction approaches on the laboratory tests, the correction models were also applied to the initial heat transfer measurements of the wind tunnel experiment. Due to the corrections the systematic error in the heat flux measurements could be resolved and thereby achieving an improved consistency in the experimental results. Based on the observations, the systematic errors become relevant in situations, where different temperature levels are present in the image. Both errors depend on the amplitude of the temperature difference. The stray light artefact scales with the areal size of the temperature level, while for the readout artefact only the

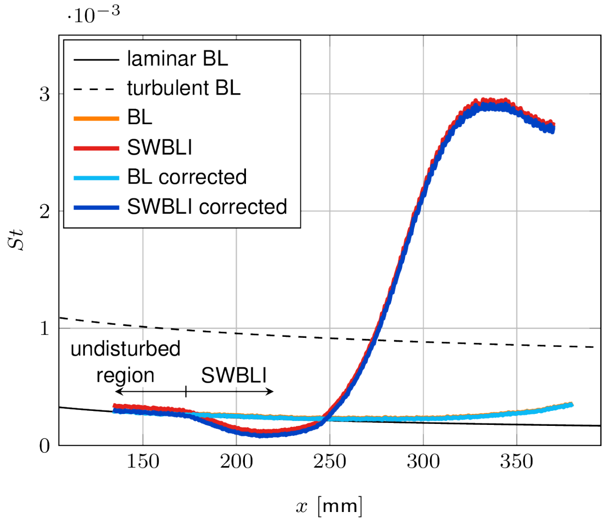

(a) *Streamwise St distribution on the flat plate with and without a SWBLI.*

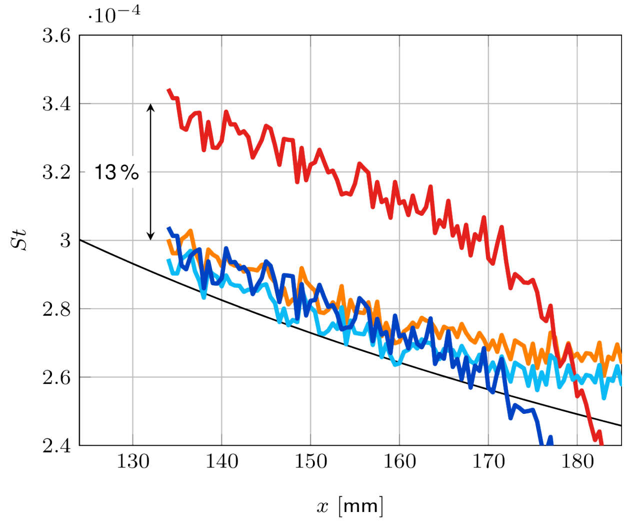

(b) *Enlarged view of figure 9a.*

Fig. 9. *St improvement due to the readout and stray light corrections.*

readout line has to be considered. Regarding the determination of heat transfer rates, the amplitude of the systematic error has to be in the same order of magnitude as the temperature difference between consecutive images to become relevant.

The systematic errors were only analyzed for the *IRCAM EQUUS 327kL* camera. If other infrared camera models are affected by the same artefacts and to what extent the elaborated correction approaches with the determined calibration parameters are transferable, must be checked in further studies.

References

[1] Nicolas Horny. FPA camera standardisation. *Infrared Physics & Technology*, 44(2):109–119, 2003.

[2] Giovanni Maria Carlomagno and Gennaro Cardone. Infrared thermography for convective heat transfer measurements. *Experiments in Fluids*, 49(6):1187–1218, 2010.

[3] Jingzhong Wang and Xiaoqing Xu. The non-uniformity correction for IRFPA. In *2009 International Conference on Computational Intelligence and Software Engineering*, pages 1–4, 2009.

[4] Brian S. Kinsey, James A. S. Threadgill, and Stuart A. Craig. Measurement of quantitative heat flux on translucent surfaces using infrared thermography. *Experiments in Fluids*, 66(101), 2025.

[5] Erich Schülein. Skin friction and heat flux measurements in shock/boundary layer interaction flows. *AIAA Journal*, 44(8):1732–1741, 2006.

[6] Erich Schülein. Effects of laminar-turbulent transition on the shock-wave/boundary-layer interaction. *AIAA 2014-3332, 44th AIAA Fluid Dynamics Conference*, jun 2014.

[7] Jens Lunte and Erich Schülein. Heat transfer amplifications in transitional shock-wave/boundary-layer interactions. *AIAA 2019-3440, AIAA Aviation 2019 Forum*, jun 2019.

[8] Jackson S. Knappen. Comprehensive stray light (flare) testing: Lessons learned. *Electronic Imaging*, 2023.

[9] Chenzhao Ben, Honghai Shen, Xiao Yu, Lingtong Meng, Huishi Cheng, and Ping Jia. Stray light analysis and suppression for an infrared fourier imaging spectrometer. *Photonics*, 11(2), 2024.

[10] Wim Ruyten. Smear correction for frame transfer charge-coupled-device cameras. *Optics Letters*, 24(13):878–880, Jul 1999.

[11] Matthew Purcell, Graeme Storm, Rachel Elliott, Daya Rasaratnam, Min Qu, Mhamed El Hachimi, Kevin Moore, Przemyslaw Dmochowsky, Derek Tolmie, John Hart, Sara Pellegrini, Lindsay Grant, and Arnaud Laflaquiere. Image artifacts caused by pixel bias cells in CMOS imagers targeted for mobile applications. *In Proceedings of the International Image Sensor Worshop*, 2009.

[12] Tomas Geurts, Bart Cremers, Manuel Innocent, Wiet Vroom, Cedric Esquenet, Thomas Cools, John Compiet, Burak Okcan, Genis Chapinal, Carl Luypaert, Nicolas Bresson, Peter Deruytere, Patrick Pintens, and Roel Aerts. A 98dB linear dynamic range, high speed CMOS image sensor. *In Proceedings of the International Image Sensor Worshop*, pages 282–285, 2017.

[13] John David Vincent, Steven E. Hodges, John Vampola, Mark Stegall, and Greg Pierce. *Fundamentals of Infrared and Visible Detector Operation and Testing*. John Wiley & Sons, Inc., 2 edition, 2015.